PRISMA NOISE COEFFICIENTS ESTIMATION

Maria Francesca Carfora [1], Raffaele Casa [2], Giovanni Laneve [3], Nada Mzid [2], Simone Pascucci [4], Stefano Pignatti [4,]*

[1] Istituto per le Applicazioni del Calcolo "M. Picone", Italian National Research Council, Naples, Italy; f.carfora@na.iac.cnr.it

[2] Department of Agriculture Forestry and Nature (DAFNE), University of Tuscia, 01100 Viterbo, Italy; nada.mzid@unitus.it; rcasa@unitus.it

[3] Scuola di Ingegneria Aerospaziale (SIA) – Sapienza University of Rome, Via Salaria, 851, 00138 Roma, Italy; giovanni.laneve@uniroma1.it

[4] Institute of Methodologies for Environmental Analysis (IMAA)- Italian National Research Council (CNR), C. da S.Loja, 85050 Tito Scalo, Italy; simone.pascucci@imaa.cnr.it; stefano.pignatti@imaa.cnr.it

IGARSS 2022 - 2022 IEEE International Geoscience and Remote Sensing Symposium | 978-1-6654-2792-0/22/$31.00 ©2022 IEEE | DOI: 10.1109/IGARSS46834.2022.9883584

ABSTRACT

The PRISMA (PRecursore IperSpettrale della Missione Applicativa) hyperspectral satellite, launched by the Italian Space Agency (ASI) is presently operational on a global scale. The mission includes the hyperspectral imager PRISMA working in the 400-2500 nm spectral range with 234 bands and a panchromatic (PAN) camera (400-750 nm). In the context of this work, we intend to determine the two noise components (photon and thermal noise) and assess SNR with an image based approach. Results show that the SNR evaluation assessed through the collected images is coherent with the mission requirements and that the PRISMA noise components, derived on the fragmented Pignola test site, in Southern Italy, are comparable to the ones derived on the Rail Road Valley calibration site.

Index Terms— PRISMA, SNR, photon noise, thermal noise

1. INTRODUCTION

PRISMA [1], [2] [3] signal, as well as all other sensors, is affected by random noise and fixed pattern noise, like striping. Within this analysis, we assume that fixed pattern noise (coherent noise) has been already mitigated by the standard L1 procedure that convert the acquired Digital Number (DN) in TOA (Top of Atmosphere) radiances. Authors are aware that they should use L0 data (i.e. DN), but DN images are not available to scientists according to the ASI data policy. Images contain two noise typologies, photon noise and thermal noise that can be configured as: i) random noise and ii) fixed pattern noise. Striping, as well as the others fixed effects, is normally related to calibration error and it should be minimized at the time of the radiometric calibration (i.e. L1 processing). For random noise the additive model [4], [5] is widely used. It assumes independence between the useful signal and the noise. The work of [6], based on the work [4], assesses the noise variance by considering a per band approach and exploiting the correlation between and within bands (i.e. spectral – spatial) via multiple linear regression (MLR). To face the difficulties to identify in Italy large enough homogenous areas, we have used an image based technique that doesn't require the selection of homogeneous areas, as in the work of [7], according to the work of [9], [10] [11]. The noise parameters (i.e. photon and thermal noise), in each band, are estimated by solving a constrained maximization problem on the noise likelihood [9].

The paper is organized as follows: in section 2 (Materials and Methods) we first provide a brief description of the PRISMA hyperspectral payload [1], [12], [13] and of the images used for this study. Then we describe the algorithms applied to retrieve the noise components as well as the SNR. In the last section we evaluate the photon and thermal noise components retrieved on the images.

2. MATERIALS AND METHODS

2.1. PRISMA mission characteristics

The PRISMA satellite (Table 1) has a ground sampling distance (GSD) of 30 m and is coupled with a co-registered high-resolution (5 m) panchromatic camera. The hyperspectral sensor covers the full range from 400 to 2500 nm with 234 spectral bands by using a prism as dispersing element. A complete PRISMA description, including optical design, technical specifications and pre-launch/in-flight spectral and radiometric characterization/calibration is given in [14] and [15].

Authorized licensed use limited to: Universita degli Studi di Napoli Federico II. Downloaded on December 27,2023 at 07:20:08 UTC from IEEE Xplore. Restrictions apply.

Table 1. Main PRISMA mission characteristics

Field of View (FOV/IFOV)	2.77° / 48.34mrad
Swath	30 km
Spectral range VSWIR	VNIR: 400–1010nm (66 bands)
	SWIR: 920–2500 nm (173 bands)
	PAN: 400–700 nm
Signal-to-noise ratio	VNIR: >160 (450 @ 650 nm)
	SWIR: >100 (>360 @ 1550 nm)
	PAN: >240
Spectral Width	≤14 nm

2.2. The PRISMA images

Two sites have been used for this work: the Rail Road Valley (RRV) that belongs to the RadCalNet (radcalnet.org). The RRV site is a dry lakebed of compacted clay-rich lacustrine deposits forming a relatively smooth surface with no vegetation with reflectance of about 0.3. RRV was selected because many images are available and for the higher spatial homogeneity useful to test the efficiency of noise coefficient retrieval algorithm tuning. Moreover, images centered in the experimental farm of Pignola (40.55730, 15.75792, 816m a.s.l.), belonging to the Lucanian Agency for Development and Innovation in Agriculture ((http://www.alsia.it), were collected to analyze the PRISMA noise behavior on a fragmented agricultural land cover. The Pignola experimental farm (about 140 ha) mainly consists of arable land, pastures, and coppice with tall trees. Table 2 lists the PRISMA acquisitions considered for this study.

Table 2. List of the PRISMA acquisition selected for this study

site	data	viewing angle
RRV	03/07/2020	4.1
Pignola	22/12/2020	-3.9
Pignola	02/07/2021	-16.5

2.3. The noise coefficient retrieval

The data flow that describes the processing is composed by 7 processing steps. They are: 1) MLR to separate useful signal and noise; 2) constrained maximization of the noise likelihood; 3) retrieval of photon and thermal noise components; 4) estimate of noise stdev and SNR; 5) image whitening; 6) constrained maximization of the noise likelihood; 7) residual noise assessment.

Under the additive noise hypothesis, the PRISMA L1 image pixel (X) in the 234 PRISMA channels can be viewed as a superposition of two vectors: the signal vector $\boldsymbol{s} = [s_1,\ldots,s_{nch}]$ and the random noise vector $N(s) = N_1(s_1),\ldots,N_{nch}(s_{nch})$ (with nch equal to the number of bands). The signal $\boldsymbol{s}$ is characterized by a significant strong spectral correlation, while the noise N, composed by photon and thermal noise, is modelled by a zero mean Gaussian random noise having the covariance function of the useful signal. Therefore, the noise variance σ_λ^2 per band is expressed as the sum of two contributions (Eq. 1), one $(\gamma_{SD,\lambda})$ linearly dependent on the signal and the second one $(\gamma_{SI,\lambda})$ assumed as signal independent.

A multiple linear regression (MLR) is used to predict the signal based on the adjacent bands on the base of the high

$$\sigma_\lambda^2(s_\lambda) = \gamma_{SD,\lambda} s_\lambda + \gamma_{SI,\lambda} \qquad 1$$

spectral correlation of the signal and the spectral uncorrelation of the random noise terms between adjacent bands [9]. Noise information is assessed by subtracting the predicted MLR signal from the L1 PRISMA image. The followed approach doesn't require spectrally homogeneous regions of interest. Each band in the subset area can be expressed by a vector having dimension equal to the number of rows x columns. Once estimated the noise variance σ_λ^2 via the MLR procedure, the spectral noise coefficients $\gamma_{SD,\lambda}$ and $\gamma_{SI,\lambda}$ are derived by a constrained maximization procedure on the "noise likelihood function", according to the study of [9].

$$\left(\hat{\Gamma}_{SD,\lambda},\, \hat{\Gamma}_{SI,\lambda}\right) = argmax_{\substack{\gamma SD,\lambda>0 \\ \gamma SI,\lambda>0}} \Lambda_\lambda\left(\gamma_{SD,\lambda}, \gamma_{SI,\lambda}\right) \qquad 2$$

The noise coefficients are found by a numerical search algorithm that maximizes the likelihood function $\Lambda_\lambda(\gamma_{SD,\lambda}, \gamma_{SI,\lambda})$ of the observed noise vector.

The obtained estimate of the noise variance in each spectral band can also be applied to derive an estimate of the SNR_λ, evaluated as the ratio between the median of the signal and the median of the noise stdv per band. Moreover, the two components $SNR_{SD,\lambda}$ and $SNR_{SI,\lambda}$ of SNR_λ can be retrieved. They measure the ratio between the signal and the noise stdv per band due to the sole signal dependent noise or the sole thermal noise, respectively. We outline that these values correspond to a "average" of the SNR for each spectral band, lower than the "peak" SNR for the same band, retrieved in [8] as the 90th percentile of the SNR distribution over the considered images.

The retrieved values of both the signal and the two noise components can be combined to provide an estimate of the standard deviation of the image noise $\widehat{\sigma_\lambda}(i)$ for each spectral band and each pixel as

$$\widehat{\sigma_\lambda}(i) = \widehat{\sigma_\lambda}(i, s_\lambda) = \sqrt{\gamma_{SD,\lambda} * \bar{s}_\lambda(i) + \gamma_{SI,\lambda}} \qquad 3$$

The noise estimate $\widehat{\sigma_\lambda}(i)$ can now be applied to whitened (rescaling) the L1 data set $X_\lambda(i)$ considering $Y_\lambda(i) = \frac{X_\lambda(i)}{\widehat{\sigma_\lambda}(i)}$. The expected noise derived by a MLR approach after the whitening should have a standard normal distribution. All deviations from this expected behavior are to be assumed as indication of residual structure in the noise component (coherent noise).

3. DISCUSSION OF THE RESULTS

Authorized licensed use limited to: Universita degli Studi di Napoli Federico II. Downloaded on December 27,2023 at 07:20:08 UTC from IEEE Xplore. Restrictions apply.

We analyzed the retrievals on the images of Table 2. RRV was used as reference scene to test the workflow and to have a comparison when applied to the fragmented scenario depicted by the Pignola scenes. 1st July 2021 and 22nd of December 2020 images of Pignola were used.
Primarily, we discuss the results on the retrieval of the two noise parameters (i.e., $\gamma_{SD,\lambda}$ and $\gamma_{SI,\lambda}$) and the SNR.

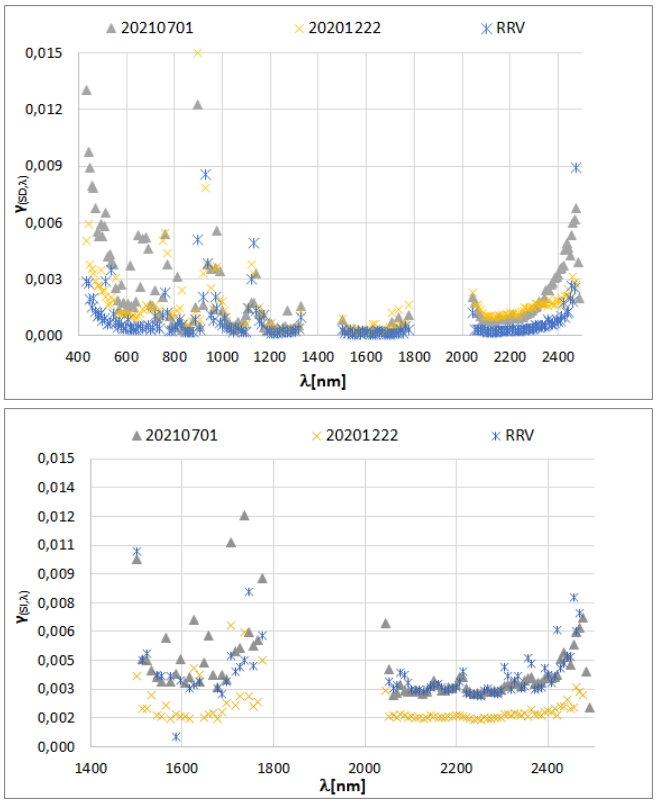

Figure 1 *top figure* $\gamma_{SD,\lambda}$ *plot versus wavelength for RRV and the Pignola images; bottom figure, just for clarity reason, subset of the* $\gamma_{SI,\lambda}$ *for the SWIR region*

The noise coefficient $\gamma_{SD,\lambda}$ depicted in Figure 1 (top) shows that the RRV assumes similar values with respect to the ones retrieved for the two Pignola images. RRV images show higher $\gamma_{SD,\lambda}$ with respect to Pignola that can be related to the higher albedo and landscape homogeneity (i.e. extremely low vegetation appears on RRV). This is particularly evident in the SWIR spectral region that is less affected by the atmospheric issues. In particular, RRV $\gamma_{SD,\lambda}$ shows values close to the December Pignola scene, in which bare outcrops of soils, dry vegetation occur, while it shows lower values with respect to the summer Pignola image in which green and crop residues diffusely occur. The $\gamma_{SI,\lambda}$ noise component in Figure 1 (bottom plot), shown just for brevity in the 1400-2500nm spectral region, assumes values higher than the ones retrieved for $\gamma_{SD,\lambda}$ in the same spectral region thus indicating that the noise variance has a dominant signal-independent component in the SWIR region.

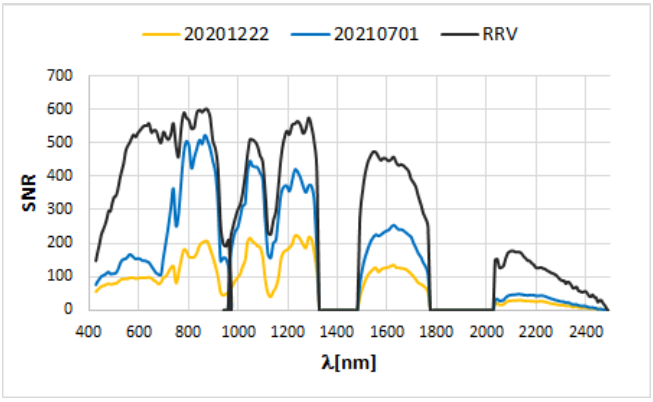

Figure 2 *SNR values depicted on RRV and Pignola sites.*

Figure 2 show that the SNR of the RRV image has a behavior similar to the one retrieved from the two Pignola images from 1000nm. As expected, winter Pignola image shows lower SNR values with respect to the summer image, while the green vegetation occurrence in the July scene cause high SNR values in the NIR. Moreover, up to 1600 nm the SNR trend is well comparable to the reference RRV image. In the SWIR, RRV, shows values sensibly higher than the Pignola ones. This difference can be anyhow explained by considering the homogeneity and the lack of green vegetation.
Finally, we analyze the residual pattern noise detected on images after the image normalization with respect to $\widehat{\sigma_\lambda}(i)$. If we analyze the spectral noise components derived by the rescaled image $Y_\lambda(i)$ with the MLR procedure, they are characterized by residual linear patterns. In the scene an evident structure is detectable mainly from lines higher than 630, based on a 1000x1000 image dimension, where a diagonal texture is evident. The presence of a similar texture has been described in [16], [17] for Landsat, and has been characterized through Fourier analysis.

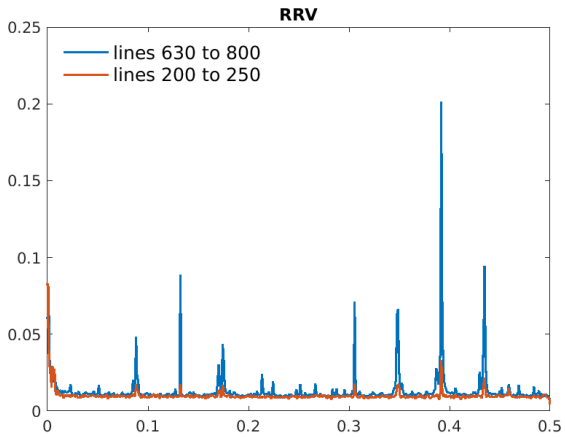

Figure 3 *Horizontally averaged FFT applied to the RRV over the selected lines of the residual noise for 823.75nm. The horizontal axis is cycles/pixel, the vertical axis shows the single-sided amplitude spectrum of the noise signal.*

Authorized licensed use limited to: Universita degli Studi di Napoli Federico II. Downloaded on December 27,2023 at 07:20:08 UTC from IEEE Xplore. Restrictions apply.

Figure 3 depicts the horizontal FFT applied to lines 630 to 800 of the RRV image and shows, along with minor disturbances, a clear spike at 0.4 cycles/pixel. This spike indicates a spatial pattern with a period of about 3 pixels in the considered region. It can be clearly seen how this coherent disturbance affects mainly the lower part of the image. The same analysis in the Fourier domain on the Pignola images highlighted the presence of the same spatial pattern in the lower part of each image with similar periodicity (about 3 pixels).

4. CONCLUSION

Noise behavior in PRISMA imagery has been evaluated by applying an image based MLR procedure to separate the useful signal from the noise along with a constrained maximization of the noise likelihood. The analysis has been carried out on the RRV RadCalNet site and the fragmented test site of Pignola. The two noise components, measured by the photon and thermal noise coefficients ($\gamma_{SD,\lambda}$ and $\gamma_{SI,\lambda}$) computed on the different sites appear not correlated to targets and show a spectral behavior comparable to each other, notwithstanding the RRV test site is much more homogeneous than the other. Moreover, the SNR derived from the RRV image shows a similar behavior when compared to the one derived from the Pignola images. Finally, the procedure highlighted the presence of a residual coherent horizontal pattern noise and a diagonal one from about the line 630 up. FFT applied to the lower part of the images detects a periodic disturbance at about 0.3 cycles/pixel that is present in all the analyzed images.

Further work, has to consider the use of the DN images (L0) instead of the L1 radiance images used in this manuscript. Authors will formalize this request to ASI as L0 are not regularly distributed to users. Moreover, a tentative algorithm to minimize the residual fixed pattern noise will be analyzed.

5. REFERENCES

[1] PRISMA Products Specification Document Issue 2.3 Date 12/03/2020. Italian Space Agency

[2] Pignatti, S., Palombo A., Pascucci S., Romano F., Santini F., Simoniello T., Amato U. et al. "The PRISMA hyperspectral mission: Science activities and opportunities for agriculture and land monitoring." In *2013 IEEE International Geoscience and Remote Sensing Symposium-IGARSS*, pp. 4558-4561. IEEE, 2013.

[3] Pignatti, S., Amodeo, A., Mona, L., Palombo, A., Pascucci, S., Rosoldi, M., ... & Laneve, G. 2021, July. Evaluation of the PRISMA Hyperspectral Radiance Data: The PRISCAV Project Activities in the Basilicata Region (Southern Italy). In *2021 IEEE International Geoscience and Remote Sensing Symposium IGARSS* (pp. 1390-1393). IEEE.

[4] B. C. Gao, "An operational method for estimating signal to noise ratios from data acquired with imaging spectrometers," Remote Sens. Environ., vol. 43, no. 1, pp. 23–33, Jan. 1993

[5] L.-R. Gao, B. Zhang, X. Zhang, W.-J. Zhang, and Q.-X. Tong, "A new operational method for estimating noise in hyperspectral images," IEEE Geosci. Remote Sens. Lett., vol. 5, no. 1, pp. 83–87, Jan. 2008.

[6] R. E. Roger and J. F. Arnold, "Reliably estimating the noise in AVIRIS hyperspectral images," Int. J. Remote Sens., vol. 17, no. 10, pp. 1951– 1962, Jul. 1996

[7] L. Alparone, M. Selva, B. Aiazzi, S. Baronti, F. Bufera, and L. Chiarantini, "Signal-dependent noise modelling and estimation in new generation imaging spectrometers," in Proc. 1st Workshop Hyperspectral, Image Signal Process.: Evol. Remote Sens., Aug. 2009, pp. 1–4

[8] Pignatti, S.; Amodeo, A.; Carfora, M.F.; Casa, R.; Mona, L.; Palombo, A.; Pascucci, S.; Rosoldi, M.; Santini, F.; Laneve, G. PRISMA L1 and L2 Performances within the PRISCAV Project: The Pignola Test Site in Southern Italy. Remote Sens. 2022, 14, 1985. https://doi.org/10.3390/rs14091985

[9] C.-I Chang and Q. Du, "Estimation of number of spectrally distinct signal sources in hyperspectral imagery," IEEE Trans. Geosci. Remote Sens., vol. 42, no. 3, pp. 608–619, Mar. 2004

[10] N. Acito, M. Diani and G. Corsini, "Signal-Dependent Noise Modeling and Model Parameter Estimation in Hyperspectral Images," in IEEE Transactions on Geoscience and Remote Sensing, vol. 49, no. 8, pp. 2957-2971, Aug. 2011, doi: 10.1109/TGRS.2011.2110657.

[11] Bioucas-Dias, J. M., & Nascimento, J. M., 2008. Hyperspectral subspace identification. IEEE Transactions on Geoscience and Remote Sensing, 46(8), 2435-2445.

[12] Coppo, P.; Brandani, F.; Faraci, M.; Sarti, F.; Dami, M.; Chiarantini, L.; Ponticelli, B.; Giunti, L.; Fossati, E.; Cosi, M. Leonardo spaceborne infrared payloads for Earth observation: SLSTRs for Copernicus Sentinel 3 and PRISMA hyperspectral camera for PRISMA satellite. Appl. Opt. 2020, 59, 6888–6901.

[13] Pignatti, Stefano, Angelo Palombo, Simone Pascucci, Filomena Romano, Federico Santini, Tiziana Simoniello, Amato Umberto et al. "The PRISMA hyperspectral mission: Science activities and opportunities for agriculture and land monitoring." In 2013 IEEE International Geoscience and Remote Sensing Symposium-IGARSS, pp. 4558-4561. IEEE, 2013.

[14] Green, R.O., Mahowald, N., Ung, C., Thompson, D.R., Bator, L., Bennet, M., Zan, J., 2020. The earth surface mineral dust source investigation: an earth science imaging spectroscopy mission. In: IEEE Aerospace Conference Proceedings. IEEE Computer Society. https://doi.org/10.1109/AERO47225.2020.9172731.

[15] Lee, C.M., Cable, M.L., Hook, S.J., Green, R.O., Ustin, S.L., Mandl, D.J., Middleton, E.M., 2015. An introduction to the NASA Hyperspectral InfraRed Imager (HyspIRI) mission and preparatory activities. Remote Sens. Environ. 167, 6–19. https://doi.org/10.1016/j.rse.2015.06.012

[16] R. Bernstein, J. B. Lotspoech, H. J. Myers, H. G. Kolsky and R. D. Lees, "Analysis And Processing of LANDSAT-4 Sensor Data Using Advanced Image Processing Techniques And Technologies," in IEEE Transactions on Geoscience and Remote Sensing, vol. GE-22, no. 3, pp. 192-221, May 1984, doi: 10.1109/TGRS.1984.350594.

[17] D. L. Helder and T. A. Ruggles, "Landsat thematic mapper reflective-band radiometric artifacts," in IEEE Transactions on Geoscience and Remote Sensing, vol. 42, no. 12, pp. 2704-2716, Dec. 2004, doi: 10.1109/TGRS.2004.839087.

Authorized licensed use limited to: Universita degli Studi di Napoli Federico II. Downloaded on December 27,2023 at 07:20:08 UTC from IEEE Xplore. Restrictions apply.